Chemical Engineering Journal 500 (2024) 157087

Contents lists available at ScienceDirect

Chemical Engineering Journal

journal homepage: www.elsevier.com/locate/cej

Boosting the electron transfer efficiency of Fe^{3+}/Fe^{2+} cycle in electro-Fenton process using molybdenum: Performance and DFT study

Yanyu Zhang [a,b], Enric Brillas [a], Aimin Wang [b], Ignasi Sirés [a,*]

[a] Laboratori d'Electroquímica dels Materials i del Medi Ambient, Departament de Ciència de Materials i Química Física, Secció de Química Física, Facultat de Química, Universitat de Barcelona, Martí i Franquès 1-11, 08028 Barcelona, Spain
[b] Beijing Key Laboratory of Aqueous Typical Pollutants Control and Water Quality Safeguard, School of Environment, Beijing Jiaotong University, Beijing 100044, China

ARTICLE INFO

Keywords:
Cocatalysts
Electro-Fenton process
Pharmaceutical pollutant
Radical oxidants
Singlet oxygen

ABSTRACT

A novel coupling of a gas-diffusion electrode (GDE)-based electro-Fenton (EF) system, using Fe^{3+} and Mo powder as cocatalysts, is investigated. The proposed EF-Fe^{3+}/Mo process enhanced the Fe^{3+}/Fe^{2+} cycle, ensuring the rapid consumption of electrogenerated H_2O_2. This resulted in a greater $^{\bullet}OH$ production from Fenton's reaction, yielding a quick degradation of the β-blocker acebutolol selected as model organic pollutant. DSA anode yielded complete but slightly slower drug removal as compared to BDD. The best operation conditions at pH 3.0 were: 0.5 mM Fe^{3+} and 10 mg L^{-1} Mo powder, applying a current density of 30 mA cm^{-2}. Specific scavengers disclosed the formation of $^{\bullet}OH$ from Fenton's reaction, along with $O_2^{\bullet-}$ and $^1O_2$ at the Mo surface. Surface analysis by SEM, XRD, and XPS showed that the cycled Mo powder retained the same compact, porous, and rock-like structure as the pristine one, revealing the presence of Mo^0, Mo^{4+}, Mo^{5+} and Mo^{6+} species, which included oxides like MoO_2 and MoO_3. DFT calculations allowed the optimization of the chemical structure of acebutolol and provided information about the electrostatic potential distribution and the HOMO/LUMO levels. From this, the sites prone to nucleophilic and electrophilic attack from reactive oxygen species were elucidated, and a reaction sequence for acebutolol degradation is finally proposed from the by-products detected by GC–MS.

1. Introduction

Over the last decade, the electro-Fenton (EF) process has been recognized as one of the most popular electrochemical advanced oxidation processes (EAOPs), owing to its outstanding ability to generate highly oxidizing hydroxyl radicals ($E°(^{\bullet}OH/H_2O) = 2.8$ V/SHE), which can non-selectively degrade recalcitrant organic pollutants [1–3]. A notable feature of the EF process is the continuous *in situ* production of hydrogen peroxide (H_2O_2) via two-electron oxygen reduction reaction (1). This enables a continuous flow of $^{\bullet}OH$ generated from Fenton's reaction (2), which occurs in the presence of added Fe^{2+} [4,5]. Furthermore, in EF systems, this ion can be efficiently regenerated via cathodic reduction (reaction (3)), thus enhancing the process sustainability [6]. The effective H_2O_2 generation and Fe^{2+} regeneration become pivotal factors to attain high degradation efficiencies in EF [7].

$$O_2 + 2H^+ + 2e^- \rightarrow H_2O_2 \quad (1)$$

$$Fe^{2+} + H_2O_2 + H^+ \rightarrow Fe^{3+} + {}^{\bullet}OH + H_2O \quad (2)$$

$$Fe^{3+} + e^- \rightarrow Fe^{2+} \quad (3)$$

Advanced cathode materials with high selectivity, catalytic activity and stability are required for developing a powerful EF system for organic pollutant removal. Carbonaceous materials characterized by abundant active sites and heightened H_2O_2 selectivity have been established as prevalent cathode candidates in EF systems [8]. They include carbon felt [9], hydrophobized carbons in the form of a gas-diffusion electrode (GDE) [10], activated carbon fiber [11] and carbon foam [12], among others. The submerged cathodes usually yield lower H_2O_2 accumulation than GDEs, since the latter enhance both, mass transport and electron transfer for O_2 reduction by establishing a stable hydrophobic gas–liquid-solid three-phase interface [13,14], substantially increasing the O_2 utilization efficiency [7]. The generated H_2O_2 can be readily activated by Fe^{2+}, but the generated Fe^{3+} in the solution may undergo limited adsorption because of the hydrophobicity of GDE, which can negatively affect the subsequent Fe^{2+} recycling. Note that H_2O_2 can also potentially serve as an electron donor for Fe^{3+} reduction to Fe^{2+} by reaction (4), producing the weaker hydroperoxyl radical

* Corresponding author.
E-mail address: i.sires@ub.edu (I. Sirés).

https://doi.org/10.1016/j.cej.2024.157087
Received 25 June 2024; Received in revised form 22 October 2024; Accepted 23 October 2024
Available online 28 October 2024

($HO_2^{\bullet}$), although the rate of that reaction significantly lags behind that of Fe^{3+} accumulation by reaction (2) [15]. Because of the occurrence of two competing cathodic reactions (H_2O_2 generation and Fe^{3+} reduction), how to efficiently catalyze both of them simultaneously is an important topic in the EF systems [16].

$$Fe^{3+} + H_2O_2 \rightarrow Fe^{2+} + HO_2^{\bullet} + H^+ \quad (4)$$

Several studies have validated that the Fe^{3+} reduction could be promoted through light irradiation [17] or ultrasound [18]. However, additional energy consumption elevates the operation expenses and hampers the practical application. The incorporation of chelating or reducing agents has been alternatively explored, since these compounds can act as electron donors to accelerate the Fe^{3+}/Fe^{2+} cycle [19]. Li et al. [20] found that highly reducing hydroxylamine could complex with Fe^{3+} to yield $Fe(NH_2OH)^{3+}$ species, with further conversion into Fe^{2+}. Other organic compounds such as ethylenediaminetetraacetic acid (EDTA) [21], ethylenediamine-*N*,*N*'-disuccinic (EDDS) acid [22] and ascorbic acid (AA) have been identified as effective agents for reducing Fe^{3+} [23]. However, these organic substances are also oxidized with $^{\bullet}OH$, diminishing the pollutant removal efficiency in EF [24], increasing the chemical costs and potentially causing secondary pollution [19]. Hence, the development of catalysts capable of efficiently and durably reducing Fe^{3+} is a promising way to upgrade the EF process.

Recent studies have highlighted the effectiveness of heterogeneous metal cocatalysts, as for example Mo-based materials such as MoS_2 [25,26], MoO_2 [27,28] and Mo powder [29,30], for Fe^{2+} regeneration in Fenton- and sulfate radical-based advanced oxidation processes (AOPs). This is explained by the modifications of the electronic structure or ionic valence state of the Mo active sites [31]. These materials are advantageous due to the minimal usage, stable performance, and recyclability. Mo^{4+} is considered as the singular catalytic active center in MoS_2 and MoO_2 [26,28], whereas Mo powder presents surface $\equiv Mo^0$, $\equiv Mo^{4+}$ and $\equiv Mo^{6+}$ sites that stabilize the Fe^{3+}/Fe^{2+} cycle. Yi et al. [29] examined the effectiveness of Mo powder in Fenton process, where H_2O_2 decomposition rate increased from 23.1 % to 55.8 %. As can be seen in reactions (5)-(9) ($E^0(Fe^{3+}|Fe^{2+})$ = 0.77 V, $E^0(Mo^{6+}|Mo^{4+})$ = 0.65 V, $E^0(O_2|O_2^{\bullet-})$ = 0.16 V, and $E^0(^1O_2|O_2^{\bullet-})$ = 0.20 V) [29,32,33], Mo powder then promotes the generation of superoxide ion ($O_2^{\bullet-}$) and singlet oxygen ($^1O_2$) in a Fenton system. This not only yields a superior Fe^{2+} regeneration, but also enriches the set of oxidizing species for enhanced pollutant degradation. Obviously, the addition of Mo powder leads to additional reagent cost; however, this material can be recycled by simple separation, and then be further reused because of its abundant reactive sites, leading to cost reduction as compared to other processes. To our knowledge, the integration of Mo powder with GDE-based EF process remains unexplored. Only Zhou et al. [34] explored such cocatalytic system in EF, although employing a granular active carbon cathode with very low H_2O_2 production as compared to GDE, and without discussing the interaction between pollutants and reactive species.

$$Fe^{3+} + \equiv Mo^0 \rightarrow Fe^{2+} + \equiv Mo^{4+} \quad (5)$$

$$2Fe^{3+} + \equiv Mo^{4+} \rightarrow 2Fe^{2+} + \equiv Mo^{6+} \quad (6)$$

$$Fe^{2+} + O_2 \rightarrow Fe^{3+} + O_2^{\bullet-} \quad (7)$$

$$Mo^0 + {}^{\bullet}OH \rightarrow \equiv Mo^{4+} + OH^- \quad (8)$$

$$\equiv Mo^{6+} + O_2^{\bullet-} \rightarrow \equiv Mo^{4+} + {}^1O_2 \quad (9)$$

The present article proposes, for the first time, the coupling of Mo powder with a GDE-based EF system to enhance the Fe^{3+}/Fe^{2+} cycle. An Fe(III) salt was used as the iron source, aiming to produce not only $^{\bullet}OH$ but also $O_2^{\bullet-}$ and $^1O_2$, being more suitable because of its lower industrial cost and larger stability during storage. Also, the use of Fe(III) salt helped to demonstrate the sluggish Fe^{2+}/Fe^{3+} cycle in EF system and examine the enhancement originated from the use of Mo powder. The β-blocker acebutolol was selected as drug pollutant, since it is frequently detected in wastewater treatment plants [35] and surface water [36]. The influence of the anode, current density (*j*), Mo dosage, and Fe^{3+} concentration on pollutant degradation in this novel EF-Fe^{3+}/Mo process was assessed. The stability and reusability of the Mo powder was analyzed by conventional methods and the production of reactive species was confirmed by specific quenching experiments. Based on this, the interaction between the generated reactive species and acebutolol was evaluated by density functional theory (DFT) calculations. Finally, the by-products formed were detected and a reaction sequence for acebutolol degradation is proposed.

2. Materials and methods

2.1. Chemicals

Commercial molybdenum powder (99.9 %, CAS: 7439–98-7, particle size 2–4 μm) was purchased from Alfa-Aesar. Analytical grade acebutolol hydrochloride (CAS: 34381–68-5), iron(III) perchlorate hydrate, 2,2,6,6-tetramethylpiperidine (TEMP), *tert*-butyl alcohol (TBA), *p*-benzoquinone (*p*-BQ), ascorbic acid, 1,10-phenantroline and technical grade titanium(IV) oxysulfate were purchased from Sigma-Aldrich. HPLC grade acetonitrile and dichloromethane were supplied by Panreac. Analytical grade anhydrous sodium sulfate, sulfuric acid, potassium dihydrogen phosphate, acetic acid and sodium hydroxide were purchased from Merck, Panreac and J.T. Baker. All solutions were prepared with ultrapure water (18.2 MΩ cm at 25 °C) from a Merck Millipore Milli-Q system.

2.2. Electrolytic trials

The experiments were performed in an undivided jacketed glass cell. Unless otherwise stated, 150 mL of solutions at pH 3.0 were treated at 25 °C keeping magnetic stirring at 700 rpm. The anode was a 3 cm^2 DSA (DSA®-Cl_2) electrode purchased from NMT Electrodes (Pinetown, South Africa) or a boron-doped diamond (BDD) from NeoCoat (La Chaud-de-Fonds, Switzerland). The cathode was a 3 cm^2 GDE purchased from Sainergy Fuel Cell (Chennai, India) that was fed with 36 L h^{-1} air for H_2O_2 generation or 36 L h^{-1} N_2 for quenching H_2O_2. In order to remove the organic and inorganic impurities from the GDE surface, adsorbed during its production and storage, a fresh cathode was activated before first use. The surface activation was achieved by electrolyzing 150 mL of 0.050 M Na_2SO_4 solution at pH 3.0 and 25 °C, employing a DSA plate as the anode at j = 100 mA cm^{-2} for 60 min. The distance between both electrodes was 1 cm. All experiments were conducted in 0.050 M Na_2SO_4 solution as background electrolyte, and acebutolol was spiked at a concentration of 0.046 mM to examine the oxidation efficiency of different processes. Except for the experiments about the influence of reagents dosage, 0.50 mM Fe^{3+} and 10 mg L^{-1} Mo powder were added as catalysts to the solution prior to the electrolysis. The current was supplied by an Amel 2051 potentiostat–galvanostat, coupled to a Demestres 605 multimeter for cell voltage measurement.

2.3. Analytical methods

The solution pH was measured with a Crison GLP 22 pH-meter. Before analysis, all the samples were filtered with Whatman 0.45 μm PTFE syringe filters. The concentration of H_2O_2 was determined by adding titanium(IV) oxysulfate to the aliquots and measuring the absorbance of the generated complex by spectrophotometry at λ = 408 nm using a Shimadzu UV-1800 spectrophotometer [37]. The corresponding current efficiency (CE) for H_2O_2 accumulation was calculated by Eq. (10) [13].

$$CE(\%) = \frac{nFc(H_2O_2)V_s}{1000M(H_2O_2)Q}100 \quad (10)$$

where n (= 2) is the stoichiometric number of electrons transferred for oxygen reduction to H_2O_2, F is the Faraday constant (96 487C mol^{-1}), c (H_2O_2) is the concentration of accumulated H_2O_2 (mg L^{-1}), V_s is the volume of the treated solution (L), 1000 is a conversion factor, M(H_2O_2) is the molecular weight of H_2O_2 (= 34 g mol^{-1}), and Q is the charge consumed during the electrolysis.

The same spectrophotometer was used for the determination of the iron species The contents of dissolved Fe^{2+} were quantified from the absorbance of its complex with 1,10-phenantroline at λ = 508 nm, whereas the concentration of total dissolved iron was monitored by adding ascorbic acid into the sample to reduce all the iron species to Fe^{2+} [22]. The concentration of dissolved Mo ions was identified using a 5110VDV inductively coupled plasma optical emission spectrometer (ICP-OES, Agilent, USA). The acebutolol concentration was determined by reversed phase-high-performance liquid chromatography (HPLC) using a Waters 600 LC coupled with a Waters 996 photodiode array ser at λ = 235 nm. The LC was equipped with a BDS Hypersil C18 6 μm (250 mm × 4.6 mm) column at 35 °C, using a 40:60 (v/v) acetonitrile/water (10 mM KH_2PO_4 at pH 3.0) as mobile phase at 1.0 mL min^{-1}. The retention time for acebutolol was of 4.6 min. From the concentrations determined in a given assay, their pseudo-first-order kinetic analysis was performed using Eq. (11):

$$\ln\left(\frac{c_0}{c}\right) = k_1 t \tag{11}$$

where c_0 and c account for the initial drug concentration and that at time t (min) and k_1 is the pseudo-first-order rate constant (min^{-1}). In all cases, average values of duplicate experiments are given and their error bars with a confidence interval of 95 % are shown in figures.

Gas chromatography-mass spectrometry (GC–MS) was used to identify the primary generated organic products, after their extraction with CH_2Cl_2 (3 × 10 mL) followed by its volume reduction down to 1 mL. An Agilent Technologies system composed of a 7890A gas chromatograph equipped with a 5975C mass spectrometer in EI mode at 70 eV was used, equipped with a non-polar HP-5MS (30 m × 250 μm, 0.25 μm) or a polar HP-Innowax (60 m × 250 μm, 0.25 μm) column. The detailed method for the GC–MS analysis has been described elsewhere [38] and the mass spectra obtained were elucidated by comparison with those reported in the NIST11 MS database.

2.4. Catalyst characterization

Mo powder collected after 120 min of EF treatment was washed with water for 3 times, filtered through 0.22 μm PES membrane under vacuum and dried at room temperature for recycling and characterization, as compared to pristine Mo powder. The surface morphology and elemental distribution were observed by scanning electron microscopy (SEM) using a Zeiss Gemini 300 microscope combined with energy dispersive spectroscopy (EDS) using a Zeiss Smart EDX equipment. All SEM images were recorded at a voltage of 20.0 kV. For EDS-mapping, the acceleration voltage was 0.2–30 kV (10 V step variable). The structural integrity was carried out using a Rigaku ultima IV multifunctional XRD, operating at a scan voltage of 3 kV within the range of 10-80°.

X-ray photoelectron spectroscopy (XPS) analysis was performed on a Thermo Scientific K-Alpha + spectrometer. It was equipped with a mono Kα X-ray source (1486.6 eV) at an operation pressure of 5×10^{-9} mbar. The pass energy used for survey spectra was 150 eV, and 50 eV were applied to obtain the high-resolution core-level spectra. All core lines were corrected at C 1s (C-C) core line, assumed as 284.8 eV. Data were processed with the Avantage software.

2.5. Theoretical calculation methods

All DFT calculations were carried out using the Gaussian 16 program package [39]. The B3LYP [40,41] density functional method with the D3 (BJ) dispersion correction [42] was always employed. The 6–31 g(d,p) [43] basis set was used for the atoms in geometry optimizations using the PCM model with water as the solvent [44]. Vibrational frequency analyses at the same level of theory were performed to characterize stationary points as local minima without any imaginary frequencies. The condensed Fukui index from natural population analysis (NPA) charge was used for predicting the reactive sites of electrophilic and nucleophilic attack over acebutolol [45]. Detailed information about condensed Fukui index is summarized in Text S1 of SI. Orbitals analysis was accomplished with Multiwfn 3.8 (dev) [46] and VMD 1.9.3 software [47].

3. Results and discussion

3.1. H_2O_2 accumulation in the EF-Fe^{3+}/Mo system

First, several assays were made with 150 mL of 0.050 M Na_2SO_4 solution at pH 3.0 and 25 °C, at different contents of Mo powder and Fe^{3+} as cocatalysts. A cell equipped with a DSA and a GDE fed with 36 L h^{-1} O_2 as anode and cathode, respectively, was employed at moderate j = 30 mA cm^{-2}. Acidic pH was chosen because it is optimal for Fenton's reaction (2), and hence, to ensure a quick pollutant abatement [13]. The acidic pH caused the dissolution of a small amount of oxide (i.e.,

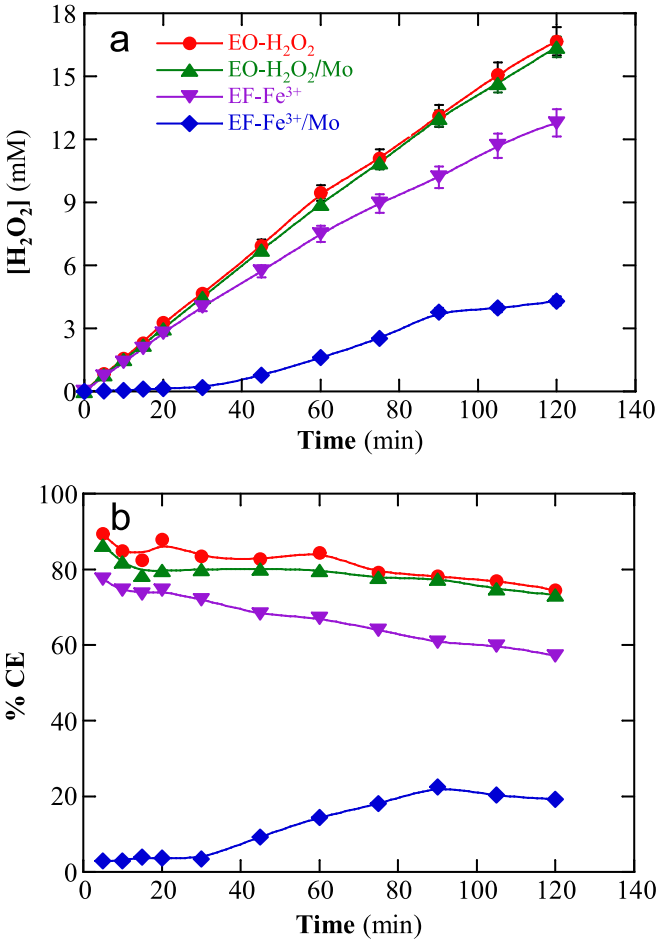

Fig. 1. (a) Evolution of accumulated H_2O_2 concentration and (b) corresponding current efficiency during the electrolysis of 150 mL of 0.050 M Na_2SO_4 solution at pH 3.0 and 25 °C under optimum conditions (10 mg L^{-1} Mo powder and/or 0.5 mM Fe^{3+}). EO, EO-H_2O_2, and EF processes were compared using an undivided electrolytic cell equipped with a DSA and a GDE as the anode and cathode, respectively, with an air flow rate of 36 L h^{-1} and current density (j) of 30 mA cm^{-2}.

detection of 0.05 mg L^{-1} Mo) covering the catalyst surface, thus enhancing the exposure of reactive sites. This also confirmed that Mo powder was stable in acidic pH and the catalysis of Fe^{2+}/Fe^{3+} cycle mainly took place on Mo surface rather than in solution. Since the lowest H_2O_2 accumulation was obtained by adding 10 mg L^{-1} of Mo powder and 0.5 mM of Fe^{3+} (data not shown), these catalyst concentrations were fixed for subsequent trials.

Fig. 1 shows that the best H_2O_2 accumulation was achieved in electrochemical oxidation (EO) with electrogenerated H_2O_2, in the absence and presence of 10 mg L^{-1} Mo powder. In both cases, a gradual increase in the H_2O_2 concentration can be observed, attaining up to 16.5 mM at 120 min. When 0.5 mM Fe^{3+} was added to the drug solution without Mo powder, the occurrence of EF-like process yielded a slightly slower H_2O_2 accumulation, achieving a lower concentration of 12.8 mM due to the oxidation of this oxidant according to reaction (4), with an expected low rate [15]. Conversely, in an analogous experiment but in the presence of Mo powder (= 10 mg L^{-1}), a dramatic H_2O_2 decay down to 4.3 mM can be observed, which can be attributed to the large generation of Fe^{2+} from reactions (5) and (6) that largely decomposes the H_2O_2 via Fenton's reaction (2). This finding makes evident that the EF-Fe^{3+}/Mo process is able to generate strong oxidants that may serve to destroy organic pollutants.

Fig. 1b depicts the change of the current efficiency for H_2O_2 accumulation with electrolysis time for the above assays. As can be seen, high CE values were obtained for the two EO-H_2O_2 processes (i.e., without and with Mo powder) starting from 86-89 % and slightly dropping down to 73–74 % at 120 min. This decay can be ascribed to the anodic oxidation of H_2O_2 at the DSA surface by reaction (12) [1]:

$$DSA + H_2O_2 \rightarrow DSA(HO_2^{\bullet}) + e^- + H^+ \quad (12)$$

In the EF-Fe^{3+} process, a similar trend occurred with a CE drop from 77 % down to 57 %. A different behavior can be observed for the EF-Fe^{3+}/Mo one, because a maximum CE of only 22 % was obtained at 90 min, finally dropping to 19 % at 120 min. This trend suggests a fast oxidation of the low contents of the initially generated H_2O_2 under the action of reaction (2), which progressively diminished with raising H_2O_2 content until its maximum CE value was reached. At longer times, it is also removed by reaction (5), thus slowly decreasing the CE to 19 %,

3.2. Evolution of Fe^{2+}

The ability of the EF-Fe^{3+}/Mo system to produce and consume Fe^{2+} was assessed with the above contents of both co-catalysts. First, the accumulated Fe^{2+} concentration was measured in a chemical experiment, in which a suspension containing 10 mg L^{-1} Mo powder and 0.5 mM Fe^{3+} was simply stirred without applied current. Fig. 2a shows a continuous increase in Fe^{2+} content up to 22 mg L^{-1} (0.39 mM) at 120 min, evidencing the high rate of reactions (5) and (6) to generate this ion in the absence of H_2O_2. The subsequent assay was made in the EO-Fe^{3+}/Mo system, combining DSA with a GDE fed with N_2 gas to prevent H_2O_2 generation. In that case, a maximum Fe^{2+} concentration of 12 mg L^{-1} (0.21 mM) was rapidly achieved in 10–15 min of electrolysis, whereupon it progressively decayed down to a steady value of 3.5 mg L^{-1} (0.062 mM) from 75 min. The initially fast Fe^{2+} accumulation caused by reactions (5) and (6) decayed due to the electrochemical oxidation of Fe^{2+} to Fe^{3+} at the DSA surface from reaction (13) [13], finally reaching a stationary state when the rate of production and destruction of the ion became equal. Other systems like EO-Fe^{3+}, EF-Fe^{3+} and EF-Fe^{3+}/Mo yielded much lower steady Fe^{2+} concentration, as shown in Fig. 2b. A similar steady content of 0.10 mg L^{-1} (0.002 mM) was found for the two former processes with only Fe^{3+}, informing about a similar poor reduction of this ion to Fe^{2+} at the GDE cathode via reaction (3). In contrast, when the Mo powder was present, the EF-Fe^{3+}/Mo generated more efficiently the Fe^{2+}, giving rise to a steady concentration of 0.60 mg L^{-1} (0.012 mM) as result of the more balanced generation (from

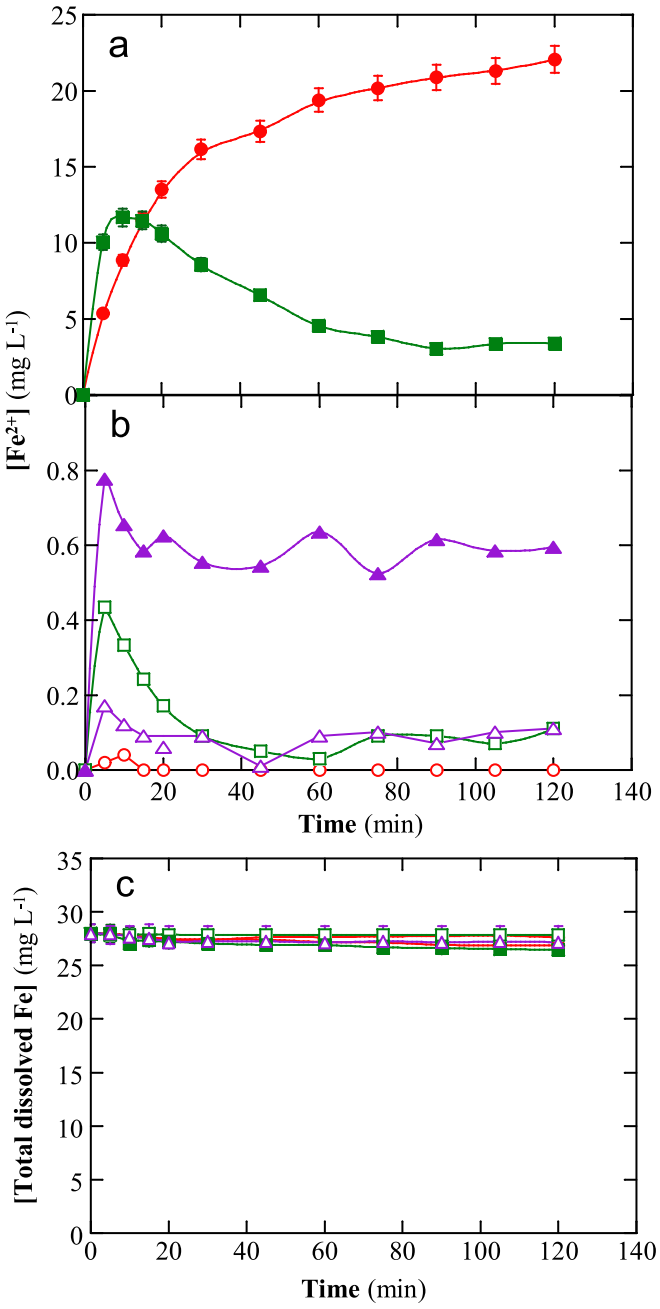

Fig. 2. Evolution of (a,b) Fe^{2+} and (c) total dissolved Fe concentrations when treating 150 mL of 0.050 M Na_2SO_4 solution with 0.5 mM Fe^{3+}, in the absence and presence of 10 mg L^{-1} Mo powder: (●) Fe^{3+}+Mo, (○) Fe^{3+}, (■) EO-Fe^{3+}/Mo, (□) EO-Fe^{3+}, (▲) EF-Fe^{3+}/Mo and (△) EF-Fe^{3+}. An undivided electrolytic cell with a DSA and a GDE as the anode and cathode, respectively, was employed at j = 10 mA cm^{-2}. The GDE cathode was fed with 36 L h^{-1} of N_2 (in EO) or air (in EF).

reactions (5) and (6)) and disappearance (from Fenton's reaction (2) and reactions (7) and (13)). This result evidences that this system is able to maintain a Fe^{2+} concentration, presumably high enough to form the largest amounts of oxidants ($^{\bullet}OH$, $O_2^{\bullet-}$ and $^1O_2$) for organic pollutant removal.

$$Fe^{2+} \rightarrow Fe^{3+} + e^- \quad (13)$$

The solubility of iron ions in the above assays carried out at pH 3.0 was also determined. Fig. 2c highlights that the initial iron concentration of 28 mg L^{-1} (0.5 mM) did not vary significantly in all trials, which

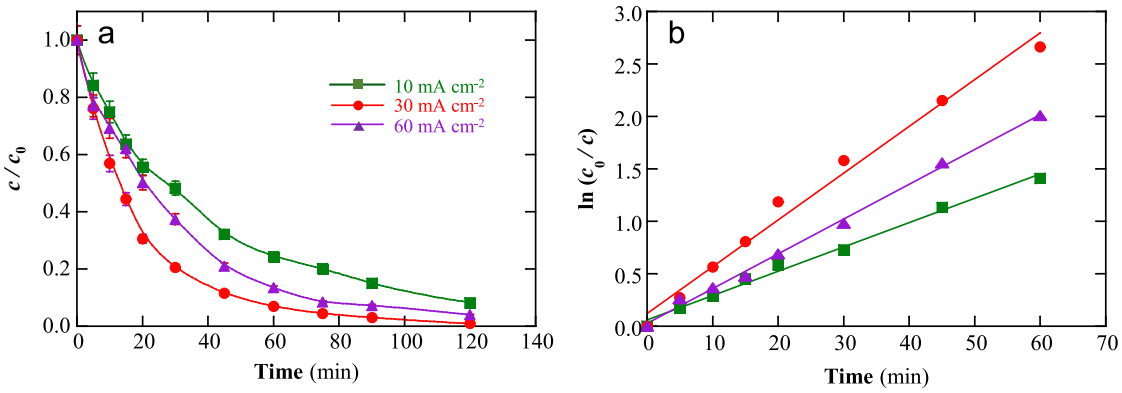

Fig. 3. Effect of applied current density on (a) normalized drug concentration decay vs. time and (b) corresponding pseudo-first-order kinetic analysis for the EF-Fe^{3+}/Mo treatments of 150 mL of 0.046 mM acebutolol + 0.050 M Na_2SO_4 solution at pH 3.0, and 25 °C, with 0.5 mM Fe^{3+} in the presence of 10 mg L^{-1} Mo powder and DSA.

Table 1
Apparent pseudo-first-order rate constants and corresponding square regression coefficients obtained for the EF-Fe^{3+}/Mo treatment of 0.046 mM acebutolol + 0.050 M Na_2SO_4 solution at pH 3.0 under different experimental conditions.

Anode	j (mA cm^{-2})	[Mo] (mg L^{-1})	[Fe^{3+}] (mM)	Scavenger	k_1 (10^{-2} min^{-1})	R^2
BDD	30	—	0.5	—	3.55	0.998
		10	0.5	—	7.53	0.992
DSA	10	10	0.5	—	2.32	0.996
	30	—	—	—	0.40 [a]	0.986 [a]
		—	0.5	—	1.32	0.953
		5	0.5	—	2.91	0.976
		10	0.1	—	0.83	0.995
			0.25	—	1.40	0.997
			0.5	—	4.46 [b]	0.993 [b]
				—	4.56 [c]	0.981 [c]
				—	4.37 [d]	0.991 [d]
				5 mM TEMP	1.03	0.969
				10 mM TEMP	0.85	0.995
				5 mM TBA	0.55	0.964
				10 mM TBA	0.57	0.976
				5 mM *p*-BQ	2.10	0.925
				10 mM *p*-BQ	1.23	0.965
		30	0.1	—	0.97	0.989
	60	10	0.5	—	3.31	0.998

[a] EO-H_2O_2 process.
[b] 1st cycle.
[c] 2nd cycle.
[d] 3rd cycle.

means that Fe^{2+} and Fe^{3+} do not precipitate under the experimental conditions tested. A good stability of the novel EF-Fe^{3+}/Mo can thus be inferred.

3.3. Effect of operation variables over acebutolol degradation

First, the effect of the anode on acebutolol degradation was assessed, as explained in Text S2. On the other hand, the current density is a more relevant and crucial parameter to improve the performance of the EF-Fe^{3+}/Mo treatment because it modulates the generation of oxidants. The effect of this operation variable was studied for 150 mL of 0.046 mM acebutolol + 0.050 M Na_2SO_4 solution with 10 mg L^{-1} Mo powder and 0.5 mM Fe^{3+}, at pH 3.0 and 25 °C, using a DSA/GDE cell under the application of j-values between 10 and 60 mA cm^{-2}. Fig. 3a highlights an enhanced drug decay with raising j from 10 to 30 mA cm^{-2}, as result of the increase in rate of the electrode reactions (1) and (14) that enhance the formation of H_2O_2 and DSA(•OH) and, in turn, •OH from Fenton's reaction (2). However, further rise of j to 60 mA cm^{-2} inhibited the acebutolol abatement (see Fig. 3a). This apparently surprising behavior can be ascribed to the larger acceleration of the parasitic reactions that cause the destruction of the generated oxidizing agents. Reaction (7) that occurs between Fe^{2+} and •OH is an example of such reactions. Other examples include the destruction of H_2O_2 by •OH via reaction (15) and the dimerization of the latter radical to H_2O_2 from reaction (16) [4]. Fig. 3b shows the excellent linear correlations obtained for the above assays assuming a pseudo-first-order kinetic model. As expected, the greatest k_1 = 0.0446 min^{-1} was determined at j = 30 mA cm^{-2} (see Table 1). It is noticeable that the k_1-value only grew 1.92 times when j became 3-fold higher (from 10 to 30 mA cm^{-2}), suggesting a deceleration of acebutolol removal due to the enhancement of parasitic reactions (7), (15) and (16).

$$DSA + H_2O \rightarrow DSA(^{\bullet}OH) + e^- + H^+ \quad (14)$$

$$H_2O_2 + {}^{\bullet}OH \rightarrow HO_2^{\bullet} + H_2O \quad (15)$$

$$2\,{}^{\bullet}OH \rightarrow H_2O_2 \quad (16)$$

The influence of Mo powder and Fe^{3+} dosages on acebutolol degradation profile was further examined using 150 mL of 0.046 mM drug + 0.050 M Na_2SO_4 solution at pH 3.0 and 25 °C, at the optimum j of 30 mA cm^{-2}. Fig. 4a illustrates the influence of Mo content at a fixed Fe^{3+} concentration (= 0.5 mM), showing an improvement in the decay of the normalized drug concentration as the Mo powder content was increased from 5 to 10 mg L^{-1}. In good agreement, k_1 rose from 0.0291 to 0.446 min^{-1} (see Table 1). This can be related to the acceleration of reactions (5) and (6), with higher production of Fe^{2+} and, consequently, promotion of •OH generation from Fenton's reaction (2). However, when the Mo powder dosage was risen from 10 to 30 mg L^{-1}, a dramatic deceleration of the degradation was observed (Fig. 4a), with a high drop of k_1 to 0.0097 min^{-1} because of the larger enhancement of parasitic reactions like (7), (15) and (16). It can be concluded that the concentration of 10 mg L^{-1} Mo powder was the optimal for this treatment. When the initial Fe^{3+} content grew from 0 to 0.5 mM at such optimum Mo powder dosage, a gradual rise in the acebutolol abatement (Fig. 4b) with a strong increase of k_1 (see Table 1) was found, owing to the progressive acceleration of reactions (4), (5), and (6) yielding more Fe^{2+} and hence, •OH. Total drug removal was achieved at 120 min using the highest Fe^{3+} concentration.

All the above findings allow concluding that the best treatment conditions are: 10 mg L^{-1} Mo powder and 0.5 mM Fe^{3+}. Under these conditions, the reusability of the Mo powder was assessed using the same cocatalyst in three consecutive cycles. Fig. 4c highlights the same drug decay trend in these assays, with total degradation in 120 min. Similar k_1-values, which varied between 0.0436 and 0.0457 min^{-1}, were determined as well (see Table 1). Consequently, the Mo powder was stable and reusable in the EF-Fe^{3+}/Mo process.

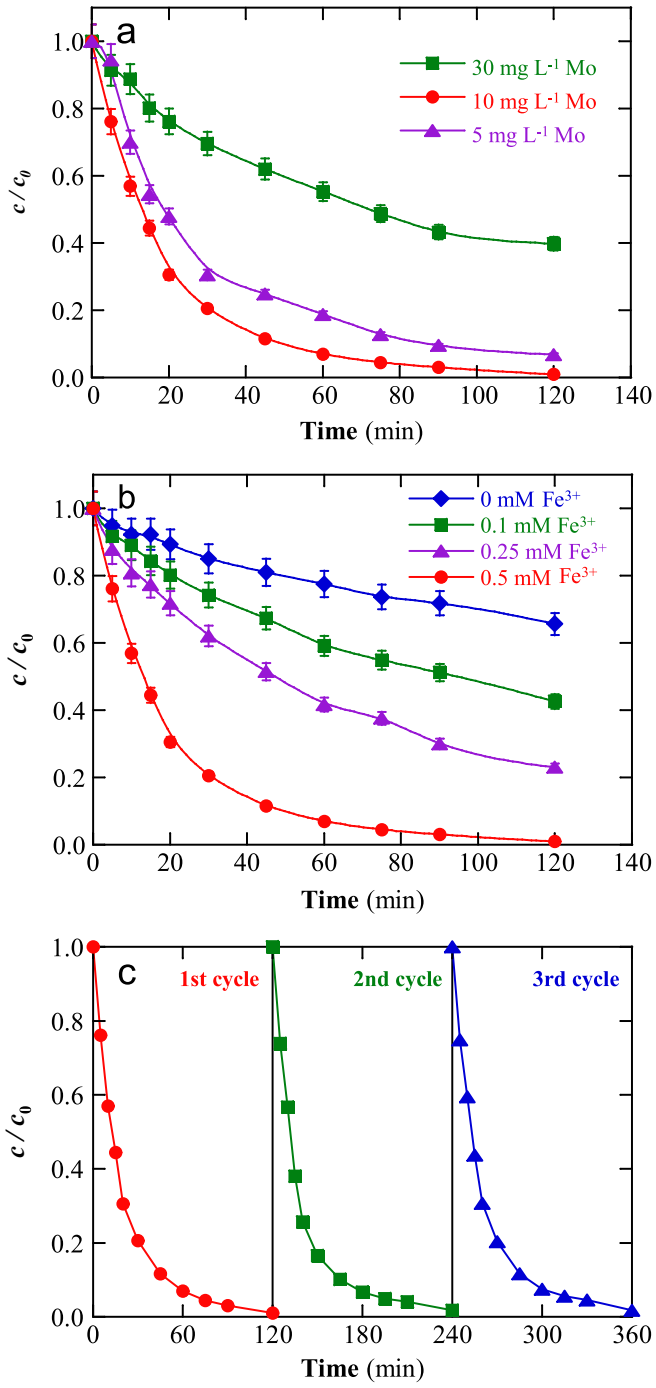

Fig. 4. Effect of (a) Mo powder and (b) Fe^{3+}concentrations over the time course of the normalized acebutolol concentration. The suspensions were treated by EF-Fe^{3+}/Mo process with DSA (see Fig. 3a). (c) Reusability tests, showing the performance in consecutive cycles with 0.5 mM Fe^{3+} and 10 mg L^{-1} Mo.

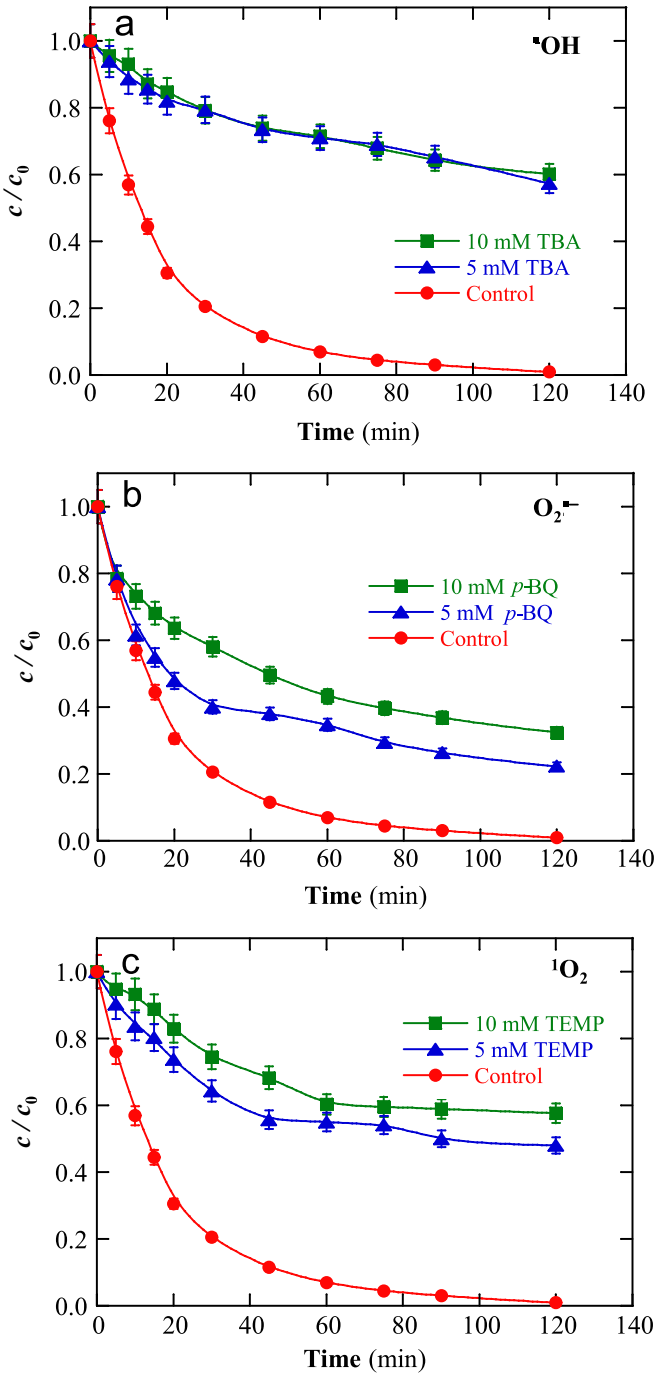

Fig. 5. Effect of (a) TBA, (b) *p*-BQ and (c) TEMP contents on the change of the normalized acebutolol concentration with time. The suspensions were treated by EF-Fe^{3+}/Mo process with DSA (see Fig. 3a).

3.4. Effect of scavengers

The production of oxidizing agents in the EF-Fe^{3+}/Mo process was confirmed by the addition of specific scavengers before performing the acebutolol electrolysis. Concentrations of 5 and 10 mM of either TBA for quenching $^{\bullet}OH$, *p*-BQ for scavenging $O_2^{\bullet-}$ or TEMP to complex $^1O_2$ were employed to avoid their contribution to oxidation. Fig. 5a depicts that both TBA contents caused a large final inhibition (60 %) of the drug abatement, with a k_1 decay down to 0.0056 min^{-1} (see Table 1), whereas Fig. 5b shows that 5 mM *p*-BQ only led to a small deceleration (22 % drug decay reduction) with $k_1 = 0.0210$ min^{-1}; the use of 10 mM *p*-BQ increased the inhibition to 32 %, with $k_1 = 0.0123$ min^{-1}. These results suggest a modest role of $O_2^{\bullet-}$ as compared to $^{\bullet}OH$ for drug removal. On the other hand, Fig. 5c reveals the inhibition of up to 48 % ($k_1 = 0.0103$ min^{-1}) using 5 mM TEMP, growing to 57 % ($k_1 = 0.0085$ min^{-1}) at 10 mM TEMP. This means that $^1O_2$ also plays an important oxidation role, which seems slightly inferior to that $^{\bullet}OH$ but much superior to that of $O_2^{\bullet-}$.

3.5. Characterization of the pristine and cycled Mo powder

SEM analysis was conducted to examine the microstructure of both fresh and cycled Mo powder. The micrographies obtained, along with the elemental mapping results, are presented in Fig. 6. The low magnification images (Fig. 6a-c) demonstrate that, after three consecutive EF-Fe^{3+}/Mo trials, the Mo powder retained a compact, rock-like structure. Generally, the particle size of the Mo catalyst was within the micron scale, ranging from 0.5 to 4.0 μm. No clear difference can be observed between the new and cycled Mo catalysts, which partially denotes its robustness. The corresponding high magnification images (Fig. 6a'-c') distinctly revealed the presence of a porous structure on the surface of the Mo powder, providing a larger specific surface area. This enhancement could be responsible for ameliorating the exposure of active site, thereby facilitating the occurrence of surface reactions in aqueous medium [48]. Hence, this would accelerate the electron transfer during the EF-Fe^{3+}/Mo treatment. EDS mapping results of Fig. 6a''-c'' illustrate the elemental distribution on the Mo surface, confirming the prevalence of Mo, along with a small amount of O. The absence of other elements suggests that the dissolved ions and molecules did not precipitate on the Mo surface, ensuring the exposure of a sufficient number of active sites for catalyzing the heterogeneous reactions.

The elemental analysis revealed that the percentage of Mo was initially low in the pristine Mo powder (51 %), but increased to 73 % and 72 % after the 1st and 3rd cycles, respectively. The relatively low initial Mo content can be attributed to the formation of molybdenum oxide when commercial Mo powder is continuously exposed to air. This oxide layer can be dissolved during the EF-Fe^{3+}/Mo treatments at pH 3.0, where 0.05 mg L^{-1} Mo can be detected in solution after 120 min electrolysis, confirming the good stability of the Mo powder. The compositional changes were further confirmed by the XRD analysis of fresh and cycled Mo powder, as depicted in Fig. 7. By comparing with standards, three typical Mo-containing species were identified: three characteristic peaks at 40.5°, 58.6°, and 73.7° were attributed to Mo (PDF#42–1120) [49], whereas shoulder peaks at 40.6°, 58.8°, and 73.9° suggested the presence of MoO_3 (PDF#47–1320), and two peaks at 36.5° and 65.7° were assigned to MoO_2 (PDF#50–0739). It is evident that the Mo^0 species, showing the highest peak intensity, predominated on the catalyst surface, whereas the intensities of MoO_3 and MoO_2 became weaker in cycled Mo powder. This observation indicates that the oxide layer was not stable during the electrolysis, resulting in increased Mo content and enhanced Mo exposure upon reuse. Considering the good reducing ability of Mo^0, a rise in active sites is expected to facilitate the Fe^{3+}/Fe^{2+} cycle and the generation of ROS in the EF-Fe^{3+}/Mo process.

XPS analysis was employed to elucidate the heterogeneous catalytic mechanism, based on the surface chemical environment and, more in particular, focusing on the evolution of Mo valence states present on the cocatalyst surface. Fig. 8 shows the deconvolution of the Mo 3d peak, evidencing contributions from Mo^0, Mo^{4+}, Mo^{5+} and Mo^{6+} orbitals. The relative content of Mo with different valence states for the fresh and cycled powder is summarized in Table 2. Interestingly, the two cycled Mo samples revealed a similar distribution pattern, which markedly differs from that of the fresh Mo powder. This change in valence proves the involvement of Mo surface in the reaction mechanism of electro-

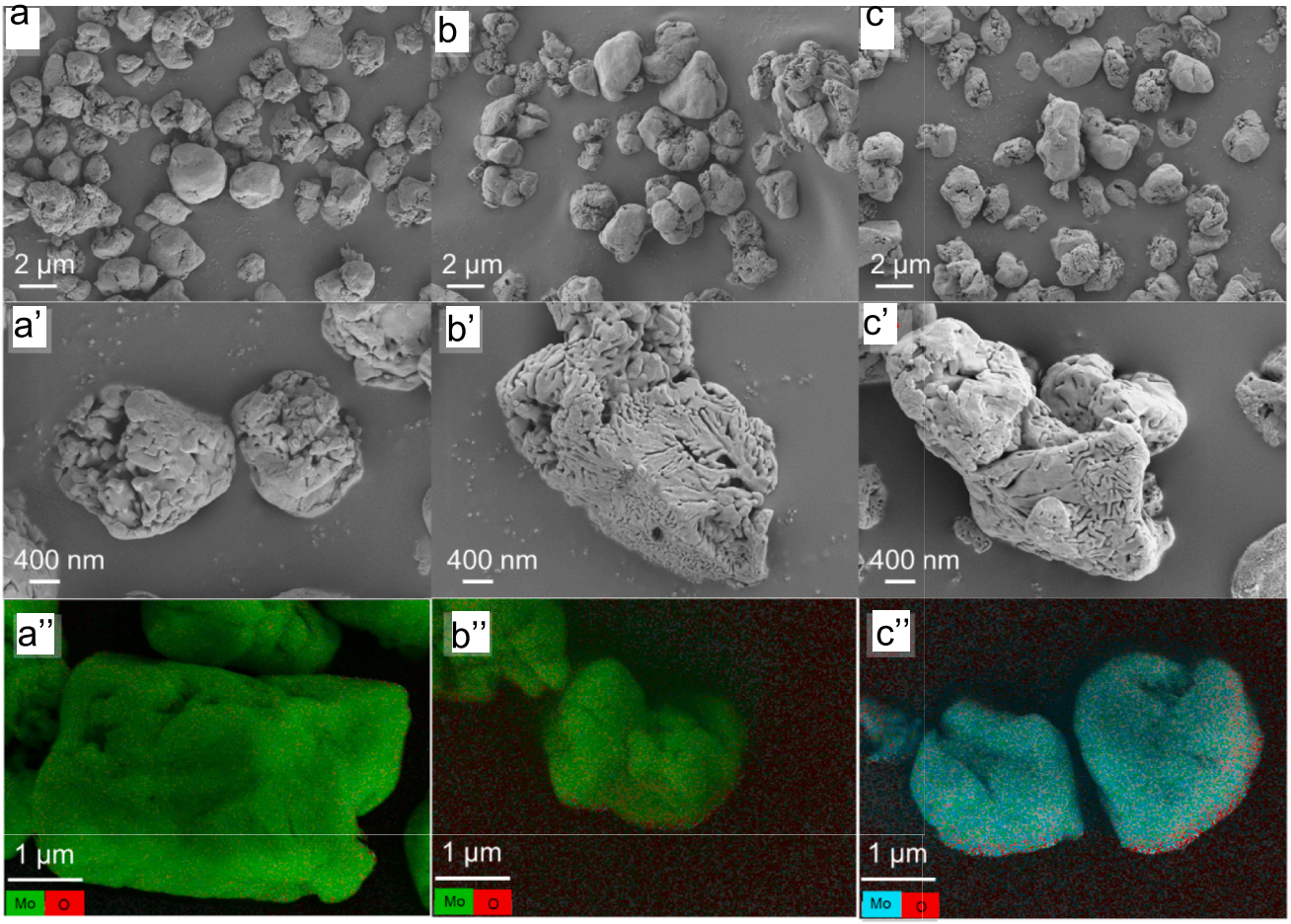

Fig. 6. SEM images of Mo powder: (a,a') Pristine, (b,b') after 1st cycle and (c,c') after 3rd cycle, analyzed at (a,b,c) low and (a',b',c') high magnification. (a'',b'',c'') Corresponding elemental mapping images showing Mo (green or blue) and O (red). (For interpretation of the references to color in this figure legend, the reader is referred to the web version of this article.)

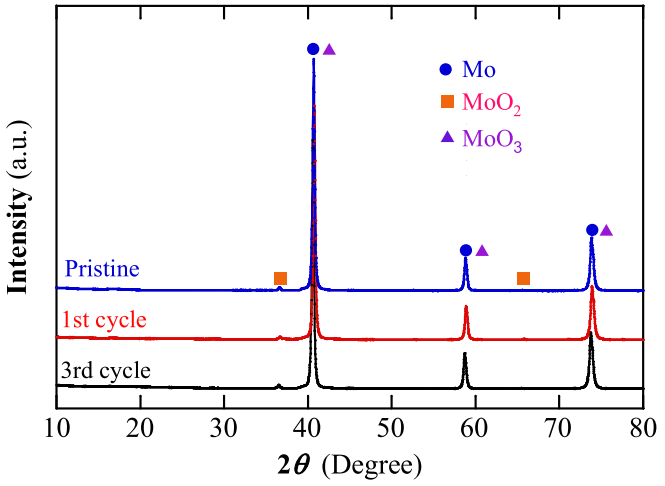

Fig. 7. XRD pattern of pristine and used Mo powder (Standard cards: PDF#42–1120 for Mo, PDF#50–0739 for MoO_2, PDF#47–1320 for MoO_3).

Fenton process, accounting for the accelerated electron transfer during Fe^{2+} regeneration. It is noteworthy that the EF-Fe^{3+}/Mo process demonstrates superior H_2O_2 accumulation owing to the triple phase boundary (i.e., gas–liquid-solid) of the GDE [50], which facilitates the rapid Fe^{3+} generation through Fenton's reaction (2). Consequently, Mo^0 and Mo^{4+} serve as the reductive reaction sites on the catalyst surface, efficiently adsorbing Fe^{3+} in the aqueous medium and donating electrons to ensure the Fe^{2+} recycling via reactions (5) and (6) [29]. In addition, Fe^{2+} regeneration may also yield Mo^{5+} by reactions (17) and (18), which can be further reduced to Mo^{4+} by Mo^0 sites (reaction (19)) [30]. This behavior explains the decrease in Mo^0 in cycled Mo compared with fresh Mo powder. Moreover, the relative content of Mo^{6+} also underwent an obvious decay, which can be attributed to the dissolution of the oxide layer and the occurrence of a series of redox reactions such as reaction (9). Therefore, an increase in the percentage of Mo^{4+} on the catalyst surface can be expected, ensuring sustainable heterogeneous catalysis on the Mo surface. The change in the valence states of Mo ions not only accelerates Fe^{2+} regeneration but also regulates the predominant ROS in advanced oxidation processes. For example, when introducing Mo to the Fenton [29] and electro-Fenton [34] systems, the contribution of $O_2^{\bullet-}$ and $^1O_2$ was reported to be superior to that of $^{\bullet}OH$. This can be due to an insufficient H_2O_2 supply that limits $^{\bullet}OH$ production, which may be consumed by exposed Mo^0 sites. At the same time, Mo^{6+} on the catalyst surface facilitates the transformation of $O_2^{\bullet-}$ into $^1O_2$ (reaction (9)), whose significant contribution to acebutolol degradation was revealed. The situation is different when a GDE is used, where enhanced H_2O_2 production guarantees the occurrence of Fenton's reaction. Hence, $^{\bullet}OH$, $O_2^{\bullet-}$ and $^1O_2$ play important roles in the EF-Fe^{3+}/Mo treatment, as confirmed above by quenching tests.

$$5Fe^{3+} + \equiv Mo^0 \rightarrow 5Fe^{2+} + \equiv Mo^{5+} \quad (17)$$

$$Fe^{3+} + \equiv Mo^{4+} \rightarrow Fe^{2+} + \equiv Mo^{5+} \quad (18)$$

$$\equiv Mo^{5+} + \equiv Mo^0 \rightarrow \equiv Mo^{4+} \quad (19)$$

3.6. DFT calculations

To investigate the relationship between the electronic structure and the sites susceptible to the attack of oxidants, DFT calculations were performed, since this allows the analysis of the acebutolol molecule at the atomic level. The optimized chemical structure, electrostatic potential (ESP) distribution, highest occupied molecular orbital (HOMO), and lowest unoccupied molecular orbital (LUMO) are summarized in

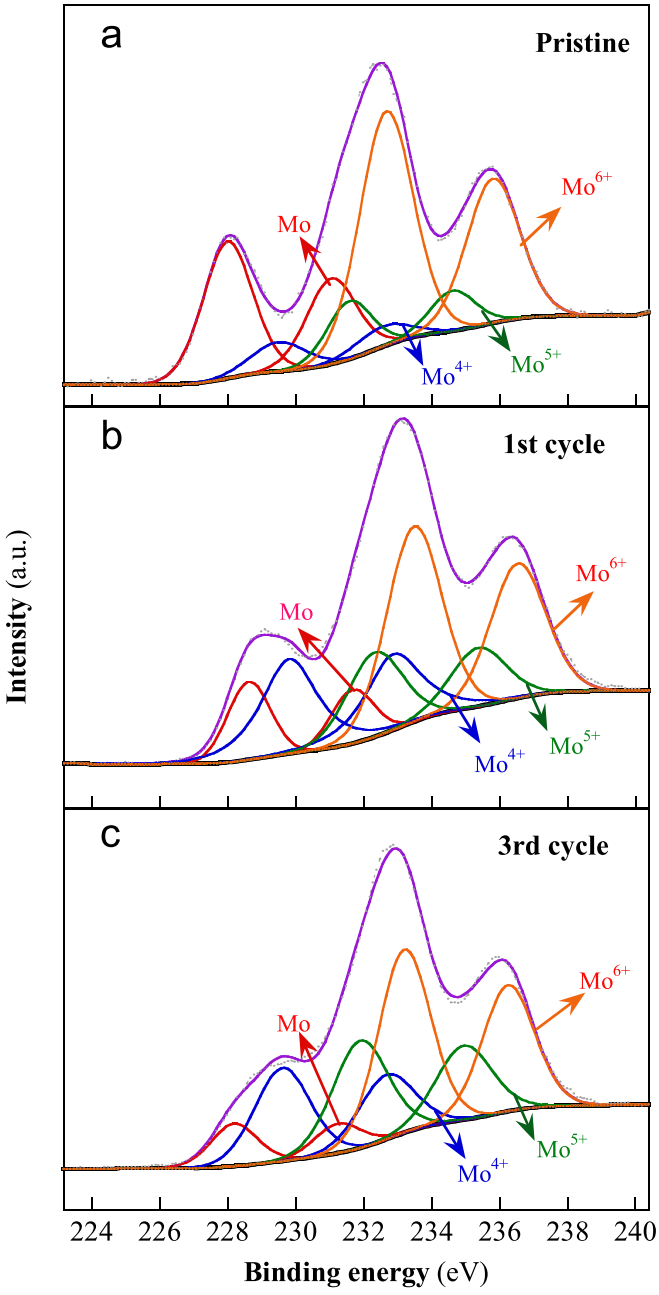

Fig. 8. High resolution XPS spectra of Mo powder showing Mo 3d: (a) Pristine, (b) after 1st cycle and (c) after 3rd cycle.

Fig. 9a-d, respectively. In general, $^{\bullet}OH$ and $^1O_2$ are identified as electrophiles in AOPs [51,52], making them more likely to attack sites that can readily lose electrons. In contrast, $O_2^{\bullet-}$ can act as both, an electrophile and a nucleophile, since its HOMO and LUMO are degenerated [53]. Compared with the conventional electro-Fenton process, EF-Fe^{3+}/Mo enriches the supply of functional ROS. The ESP distribution on the van der Waals surface (Fig. 9b) suggests that the atoms with more negative ESP can be considered as electron-rich regions, whereas

Table 2
Percentage of different valence states of surface Mo in different Mo powders.

Valence state	0	4+	5+	6+
Pristine Mo	28.8	6.8	11.1	53.4
After 1st cycle	13.2	24.0	19.0	43.8
After 3rd cycle	8.8	22.7	26.2	42.3

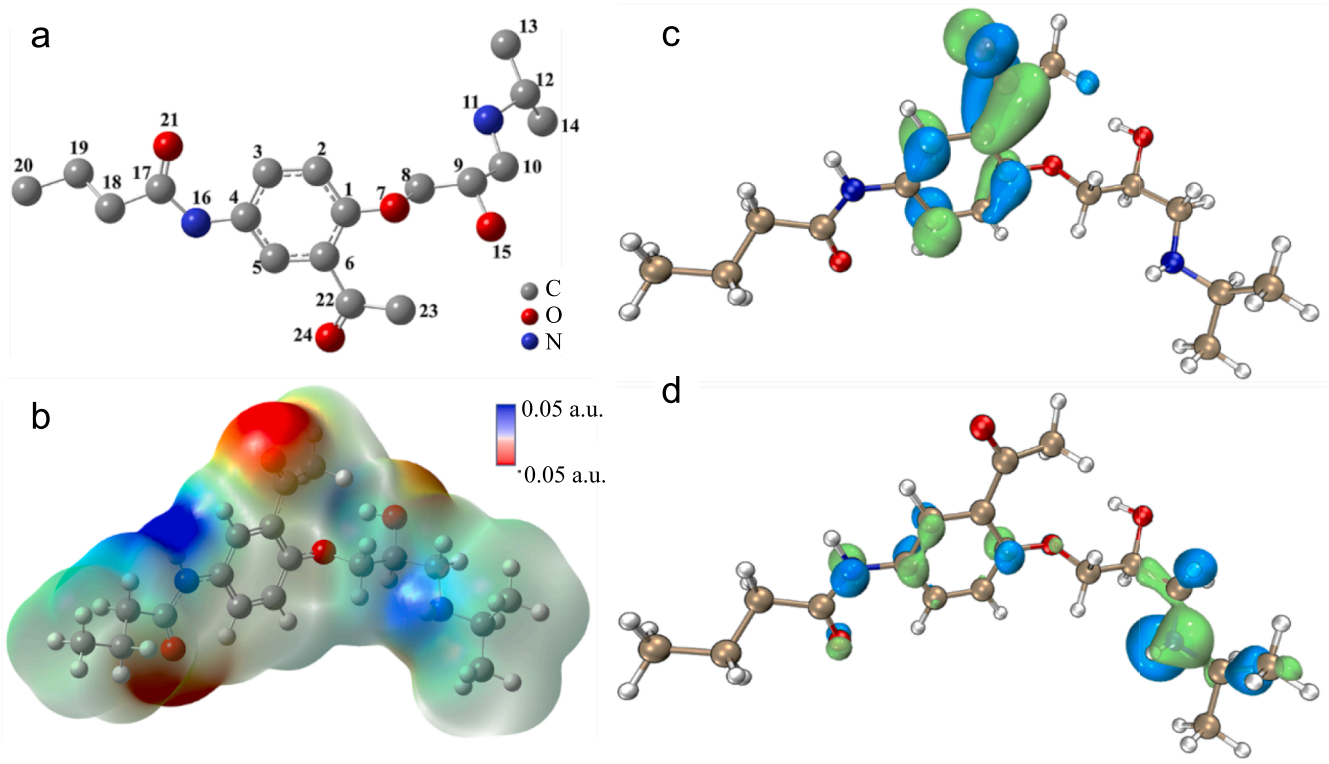

Fig. 9. (a) Chemical structure, (b) electrostatic potential (ESP) distribution, (c) highest occupied molecular orbital (HOMO) and (d) lowest unoccupied molecular orbital (LUMO) calculated for acebutolol. In (c) and (d), green and blue color account for the positive and negative phase, respectively. (For interpretation of the references to color in this figure legend, the reader is referred to the web version of this article.)

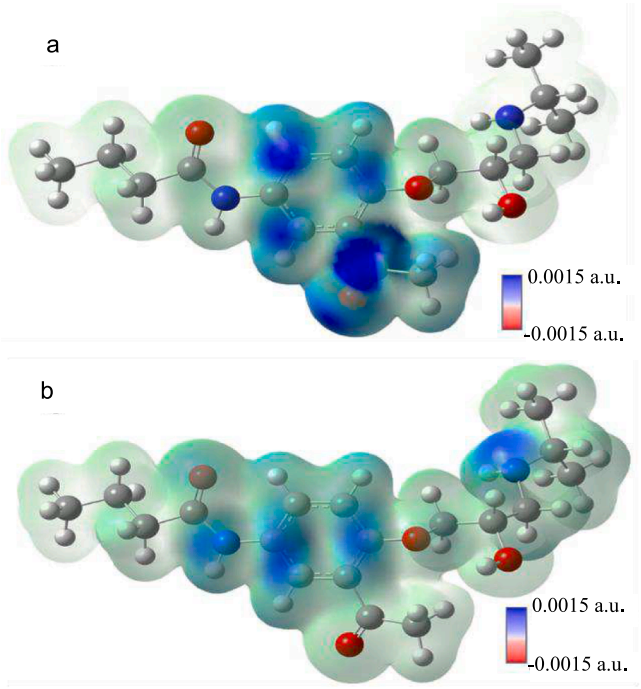

Fig. 10. Reactive sites of acebutolol for (a) nucleophilic attack and (b) electrophilic attack, as predicted by condensed Fukui indexes (f^+ and f^-).

electron-deficient regions are associated to atoms with more positive ESP, tending to attract nucleophiles [54]. Fig. 9c depicts that the HOMO of acebutolol is mainly distributed on the benzene ring and adjacent atoms, which are favorable to attract electrophiles like $^{\bullet}OH$, $O_2^{\bullet-}$ and $^1O_2$. The corresponding LUMO described in Fig. 9d suggests that these atoms tend to attract nucleophiles [55].

To further interpret the ESP results and examine the reactivity of specific atoms, the condensed Fukui indexes (f^+ and f^-) were calculated based on the natural population analysis (NPA) charge distribution, and the results are presented in Fig. 10 and Table S1. The results of Fig. 10a demonstrate that atoms with high f^+ values such as C22 ($f^+ = 0.189$), O24 ($f^+ = 0.153$), C3 ($f^+ = 0.139$), and C5 ($f^+ = 0.088$) are readily receiving electrons. Considering that these atoms also exhibit relatively high positive ESP, they can be confirmed as the predominant reactive sites for nucleophilic attack. Note that C22 and O24 are saturated sites, and the C=O bond exhibits high energy resulting from n → π* interaction [56], making it less susceptible to attack by electrophiles like $^{\bullet}OH$. This points out the importance of introducing $O_2^{\bullet-}$ in EF system, since it facilitates the generation of a series of intermediates originated from the attack on $^{\bullet}OH$-resistant C22 and O24 sites. The predominant sites for electrophilic attack with high f^- values are N11 ($f^- = 0.150$), C1 ($f^- = 0.098$), N16 ($f^- = 0.090$), C4 ($f^- = 0.075$), and O21 ($f^- = 0.075$). Since C1, C4, and O21 are saturated atoms, N11 and N16 are more vulnerable to the attack of electrophiles like $^{\bullet}OH$, $O_2^{\bullet-}$ and $^1O_2$.

3.7. Detection of by-products and proposal of a reaction sequence for acebutolol degradation

Several trials were performed with 150 mL of 0.046 mM acebutolol (**1**) + 0.050 M Na_2SO_4 solution with 10 mg L^{-1} Mo powder and 0.50 mM Fe^{3+}, at pH 3.0, 25 °C and j = 30 mA cm^{-2}. GC–MS analysis of the suspensions collected after 90 and 150 min of electrolysis revealed the formation of 10 benzenic and 4 *N*-aliphatic by-products, whose name, molecular formula, *m/z* value, chemical formula, and retention time are listed in Table S2. From these compounds, the reaction sequence for acebutolol degradation is proposed in Fig. 11, in which $^{\bullet}OH$, $O_2^{\bullet-}$ and $^1O_2$ act as oxidizing agents. As confirmed by DFT calculations, the benzene

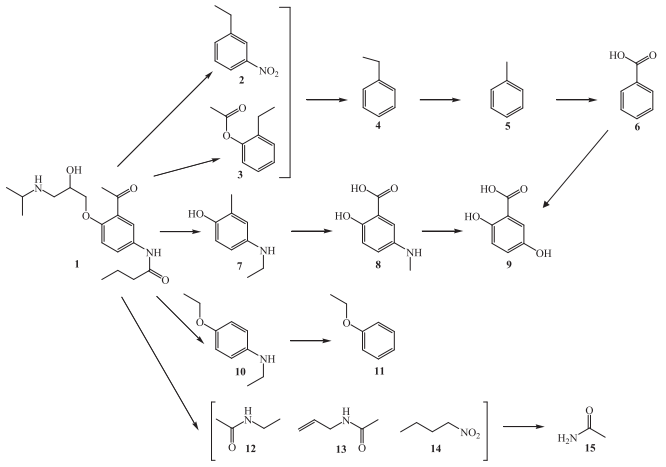

Fig. 11. Reaction sequence proposed for the degradation of acebutolol (**1**) by the EF-Fe^{3+}/Mo treatment.

ring and adjacent atoms are main reactive sites for nucleophilic or electrophilic attack. GC–MS results suggest that the initial cleavage at C22 (nucleophilic attack) and N16 sites (electrophilic attack) on the lateral groups of **1** yields the benzenic derivatives **2**, **3**, **7** and **10**. Further electrophilic oxidation of **2** and **3** yields ethylbenzene **4**, which undergoes conservative nucleophilic attack to produce toluene **5**, thereby being transformed into benzoic acid **6**. The oxidation mainly takes place on C22 and N16, predominant reaction sites for nucleophilic and electrophilic attacks, respectively. Similarly, oxidation on C22 and N16 sites on **7** leads to its carboxylation to **8**, which is subsequently hydroxylated with loss of the lateral methylamino to form 2,5-dihydroxybenzoic acid **9**. This later compound can also be formed by hydroxylation of **6**. On the other hand, compound **10** loses the lateral ethylamino group to originate ethoxybenzene **11**, resulting from the electrophilic attack on N16 site. The cleavage of the lateral amino groups of **1** lead to a mixture of N-aliphatic compounds (**12**–**14**), where the two former are oxidized to acetamide (**15**).

4. Conclusions

It has been shown that the EF-Fe^{3+}/Mo process accelerates the regeneration of Fe^{2+} from Fe^{3+}, which largely enhances the production of $^{\bullet}OH$ as the GDE ensures the continuous generation of H_2O_2 at high concentration. This results in a quick degradation of the β-blocker acebutolol. Although BDD anode yields a more rapid removal of the drug, a less expensive anode like DSA is also effective to achieve total drug degradation in this new system. The best conditions to operate at pH 3.0 were: 10 mg L^{-1} Mo powder and 0.5 mM Fe^{3+}, with applied *j* of 30 mA cm^{-2}. Higher amount of Mo powder and greater *j* were inhibitory due to the promotion of parasitic reactions. The use of specific scavengers of oxidants revealed the formation of $^{\bullet}OH$ as well as $O_2^{\bullet-}$ and $^1O_2$. SEM analysis showed that the cycled Mo powder retained the original structure. Surface analysis of the Mo cocatalyst disclosed the presence of oxides (MoO_2 and MoO_3), whereas the changes in the distribution of valence states (Mo^0, Mo^{4+}, Mo^{5+} and Mo^{6+}) demonstrated the contribution of Mo powder in the reaction mechanism of EF process. DFT analysis allowed the identification of the main sites in acebutolol susceptible to the nucleophilic and electrophilic attack of ROS. From the 10 benzenic and 4 *N*-aliphatic by-products detected by GC–MS, a reaction sequence for acebutolol degradation is finally proposed.

CRediT authorship contribution statement

Yanyu Zhang: Writing – original draft, Validation, Methodology, Investigation, Data curation, Conceptualization. **Enric Brillas:** Writing – original draft, Formal analysis. **Aimin Wang:** Project administration, Funding acquisition, Formal analysis. **Ignasi Sirés:** Writing – review & editing, Supervision, Resources, Project administration, Methodology, Funding acquisition, Formal analysis, Conceptualization.

Declaration of competing interest

The authors declare that they have no known competing financial interests or personal relationships that could have appeared to influence the work reported in this paper.

Acknowledgements

The authors kindly acknowledge support from projects PID2022-140378OB-I00 and PDC2022-133624-I00, funded by MICIU/AEI/10.13039/501100011033 (Spain), by ERDF/EU, and by the European Union NextGenerationEU/PRTR. The National Natural Science Foundation of China (NSFC, No. 51978036), as well as the PhD scholarship awarded to Y. Z. (State Scholarship Fund, CSC, China) are much appreciated as well. The expert and technical help from *Centres Científics i Tecnològics de la UB* (CCiT-UB) on GC-MS, SEM-EDS, XPS, and XRD techniques is also acknowledged.

Appendix A. Supplementary data

Supplementary data to this article can be found online at https://doi.org/10.1016/j.cej.2024.157087.

Data availability

Data will be made available on request.

References

[1] C.A. Martínez-Huitle, M.A. Rodrigo, I. Sirés, O. Scialdone, A critical review on latest innovations and future challenges of electrochemical technology for the abatement of organics in water, Appl. Catal. B: Environ. 328 (2023) 122430, https://doi.org/10.1016/j.apcatb.2023.122430.
[2] P. Xia, Z. Ye, L. Zhao, Q. Xue, S. Lanzalaco, Q. He, X. Qi, I. Sirés, Tailoring single-atom FeN_4 moieties as a robust heterogeneous catalyst for high-performance electro-Fenton treatment of organic pollutants, Appl. Catal. B: Environ. 322 (2023) 122116, https://doi.org/10.1016/j.apcatb.2022.122116.
[3] Y. Zhang, S. Miao, Y. Wang, F. Lian, X. An, H. Lan, H. Liu, J. Qu, Performance and oxidation mechanism of VUV photo–Fenton in simultaneous removal of Ni-EDTA and hypophosphite: decomplexation, low-valent phosphorous oxidation and DFT calculation, Chem. Eng. J. 485 (2024) 150148, https://doi.org/10.1016/j.cej.2024.150148.
[4] P.V. Nidheesh, S.O. Ganiyu, C.A. Martínez-Huitle, E. Mousset, H. Olvera-Vargas, C. Trellu, M. Zhou, M.A. Oturan, Recent advances in electro-Fenton process and its emerging applications, Crit. Rev. Environ. Sci. Technol. 53 (2023) 887–913, https://doi.org/10.1080/10643389.2022.2093074.
[5] A. Wang, Y. Jiang, Y. Yan, L. Bu, Z. Wei, R. Spinney, D.D. Dionysiou, R. Xiao, Mechanistic and quantitative profiling of electro-Fenton process for wastewater treatment, Water Res. 235 (2023) 119838, https://doi.org/10.1016/j.watres.2023.119838.
[6] X. Qin, P. Cao, X. Quan, K. Zhao, S. Chen, H. Yu, Y. Su, Highly efficient hydroxyl radicals production boosted by the atomically dispersed Fe and Co sites for heterogeneous electro-Fenton oxidation, Environ. Sci. Technol. 57 (2023) 2907–2917, https://doi.org/10.1021/acs.est.2c06981.
[7] Q. Zhang, M. Zhou, G. Ren, Y. Li, Y. Li, X. Du, Highly efficient electrosynthesis of hydrogen peroxide on a superhydrophobic three-phase interface by natural air diffusion, Nat. Commun. 11 (2020) 1731, https://doi.org/10.1038/s41467-020-15597-y.
[8] K.M. Nair, V. Kumaravel, S.C. Pillai, Carbonaceous cathode materials for electro-Fenton technology: Mechanism, kinetics, recent advances, opportunities and challenges, Chemosphere 269 (2021) 129325, https://doi.org/10.1016/j.chemosphere.2020.129325.
[9] H. Khan, S. Hussain, M.A. Ud Din, M. Arshad, F. Wahab, U. Hassan, A. Khan, Multiple design and modelling approaches for the optimisation of carbon felt electro-Fenton treatment of dye laden wastewater, Chemosphere 338 (2023) 139510, https://doi.org/10.1016/j.chemosphere.2023.139510.
[10] Y. Zhang, G. Daniel, S. Lanzalaco, A.A. Isse, A. Facchin, A. Wang, E. Brillas, C. Durante, I. Sirés, H_2O_2 production at gas-diffusion cathodes made from agarose-derived carbons with different textural properties for acebutolol degradation in chloride media, J. Hazard. Mater. 423 (2022) 127005, https://doi.org/10.1016/j.jhazmat.2021.127005.

[11] A. Wang, Y. Zhang, S. Han, C. Guo, Z. Wen, X. Tian, J. Li, Electro-Fenton oxidation of a β-lactam antibiotic cefoperazone: Mineralization, biodegradability and degradation mechanism, Chemosphere 270 (2021) 129486, https://doi.org/10.1016/j.chemosphere.2020.129486.

[12] S.O. Ganiyu, M.J.G. de Araújo, E.C.T. de Araújo Costa, J.E.L. Santos, E.V. dos Santos, C.A. Martínez-Huitle, S.B.C. Pergher, Design of highly efficient porous carbon foam cathode for electro-Fenton degradation of antimicrobial sulfanilamide, Appl. Catal. B: Environ. 283 (2021) 119652, https://doi.org/10.1016/j.apcatb.2020.119652.

[13] E. Brillas, I. Sirés, M.A. Oturan, Electro-Fenton process and related electrochemical technologies based on Fenton's reaction chemistry, Chem. Rev. 109 (2009) 6570–6631, https://doi.org/10.1021/cr900136g.

[14] Z. Ye, D.R.V. Guelfi, G. Álvarez, F. Alcaide, E. Brillas, I. Sirés, Enhanced electrocatalytic production of H_2O_2 at Co-based air-diffusion cathodes for the photoelectro-Fenton treatment of bronopol, Appl. Catal. B: Environ. 247 (2019) 191–199, https://doi.org/10.1016/j.apcatb.2019.01.029.

[15] M. Liu, Z. Feng, X. Luan, W. Chu, H. Zhao, G. Zhao, Accelerated Fe^{2+} regeneration in an effective electro-Fenton process by boosting internal electron transfer to a nitrogen-conjugated Fe(III) complex, Environ. Sci. Technol. 55 (2021) 6042–6051, https://doi.org/10.1021/acs.est.0c08018.

[16] F. Deng, H. Olvera-Vargas, M. Zhou, S. Qiu, I. Sirés, E. Brillas, Critical review on the mechanisms of Fe^{2+} regeneration in the electro-Fenton process: Fundamentals and boosting strategies, Chem. Rev. 123 (2023) 4635–4662, https://doi.org/10.1021/acs.chemrev.2c00684.

[17] L. Xu, L. Meng, X. Zhang, X. Mei, X. Guo, W. Li, P. Wang, L. Gan, Promoting Fe^{3+}/Fe^{2+} cycling under visible light by synergistic interactions between P25 and small amount of Fenton reagents, J. Hazard. Mater. 379 (2019) 120795, https://doi.org/10.1016/j.jhazmat.2019.120795.

[18] Y. Xu, P. Xia, C. Wang, J. Cai, H. Li, Z. Ye, H. Zhang, A mini-review on MOFs activated peroxide processes and the enhancement with the external energy, Chem. Eng. J. 462 (2023) 142021, https://doi.org/10.1016/j.cej.2023.142021.

[19] Y. Xiang, H. Liu, E. Zhu, K. Yang, D. Yuan, T. Jiao, Q. Zhang, S. Tang, Application of inorganic materials as heterogeneous cocatalyst in Fenton/Fenton-like processes for wastewater treatment, Sep. Purif. Technol. 295 (2022) 121293, https://doi.org/10.1016/j.seppur.2022.121293.

[20] D. Li, J. Yu, J. Jia, H. He, W. Shi, T. Zheng, J. Ma, Coupling electrode aeration and hydroxylamine for the enhanced electro-Fenton degradation of organic contaminant: Improving H_2O_2 generation, Fe^{3+}/Fe^{2+} cycle and N_2 selectivity, Water Res. 214 (2022) 118167, https://doi.org/10.1016/j.watres.2022.118167.

[21] X.-C. Liu, C.-S. He, Z.-Y. Shen, W.-Q. Li, N. Chen, J.-S. Song, X.-G. Zhou, Y. Mu, Mechanistic study of Fe(III) chelate reduction in a neutral electro-Fenton process, Appl. Catal. B: Environ. 278 (2020) 119347, https://doi.org/10.1016/j.apcatb.2020.119347.

[22] Z. Ye, E. Brillas, F. Centellas, P.L. Cabot, I. Sirés, Expanding the application of photoelectro-Fenton treatment to urban wastewater using the Fe(III)-EDDS complex, Water Res. 169 (2020) 115219, https://doi.org/10.1016/j.watres.2019.115219.

[23] J. Bolobajev, M. Trapido, A. Goi, Improvement in iron activation ability of alachlor Fenton-like oxidation by ascorbic acid, Chem. Eng. J. 281 (2015) 566–574, https://doi.org/10.1016/j.cej.2015.06.115.

[24] C. Wang, W. Zhang, J. Wang, P. Xia, X. Duan, Q. He, I. Sirés, Z. Ye, Accelerating Fe(III)/Fe(II) redox cycling in heterogeneous electro-Fenton process via S/Cu-mediated electron donor-shuttle regime, Appl. Catal. B: Environ. 342 (2024) 123457, https://doi.org/10.1016/j.apcatb.2023.123457.

[25] B. Sheng, F. Yang, Y. Wang, Z. Wang, Q. Li, Y. Guo, X. Lou, J. Liu, Pivotal roles of MoS_2 in boosting catalytic degradation of aqueous organic pollutants by Fe(II)/PMS, Chem. Eng. J. 375 (2019) 121989, https://doi.org/10.1016/j.cej.2019.121989.

[26] M. Xing, W. Xu, C. Dong, Y. Bai, J. Zeng, Y. Zhou, J. Zhang, Y. Yin, Metal sulfides as excellent co-catalysts for H_2O_2 decomposition in advanced oxidation processes, Chem 4 (2018) 1359–1372, https://doi.org/10.1016/j.chempr.2018.03.002.

[27] J. Ji, R.M. Aleisa, H. Duan, J. Zhang, Y. Yin, M. Xing, Metallic active sites on MoO_2 (110) surface to catalyze advanced oxidation processes for efficient pollutant removal, iScience (2020) 100861, https://doi.org/10.1016/j.isci.2020.100861.

[28] B. Shen, C. Dong, J. Ji, M. Xing, J. Zhang, Efficient Fe(III)/Fe(II) cycling triggered by MoO_2 in Fenton reaction for the degradation of dye molecules and the reduction of Cr(VI), Chin. Chem. Lett. 30 (2019) 2205–2210, https://doi.org/10.1016/j.cclet.2019.09.052.

[29] Q. Yi, J. Ji, B. Shen, C. Dong, J. Liu, J. Zhang, M. Xing, Singlet oxygen triggered by superoxide radicals in a molybdenum cocatalytic Fenton reaction with enhanced redox activity in the environment, Environ. Sci. Technol. 53 (2019) 9725–9733, https://doi.org/10.1021/acs.est.9b01676.

[30] Q. Yi, W. Liu, J. Tan, B. Yang, M. Xing, J. Zhang, Mo^0 and Mo^{4+} bimetallic reactive sites accelerating Fe^{2+}/Fe^{3+} cycling for the activation of peroxymonosulfate with significantly improved remediation of aromatic pollutants, Chemosphere 244 (2020) 125539, https://doi.org/10.1016/j.chemosphere.2019.125539.

[31] Y. Tian, M. Zhou, Y. Pan, X. Du, Q. Wang, MoS_2 as highly efficient co-catalyst enhancing the performance of Fe0 based electro-Fenton process in degradation of sulfamethazine: Approach and mechanism, Chem. Eng. J. 403 (2021) 126361, https://doi.org/10.1016/j.cej.2020.126361.

[32] C. Song, J. Zhang, Electrocatalytic oxygen reduction reaction, in: J. Zhang (Ed.), PEM Fuel Cell Electrocatalysts And Catalyst Layers: Fundamentals And Applications, Springer, London, 2008, pp. 89–134, https://doi.org/10.1007/978-1-84800-936-3_2.

[33] D.O. Whittemore, D., Langmuir, Standard electrode potential of $Fe^{3+} + e^- = Fe^{2+}$ from 5–35. deg, J. Chem. Eng. Data 17 (1972) 288–290, https://doi.org/10.1021/je60054a002.

[34] Z. Zhou, Y. Cui, Y. Huang, J. Cao, R. Wu, L. Liang, Z. Huang, The highly efficient cocatalyst of molybdenum powder enhancing low-cost and stable electro-Fenton system for organic contaminants degradation at wide pH range, J. Power Sources 520 (2022) 230860, https://doi.org/10.1016/j.jpowsour.2021.230860.

[35] M. Huerta-Fontela, M.T. Galceran, F. Ventura, Fast liquid chromatography–quadrupole-linear ion trap mass spectrometry for the analysis of pharmaceuticals and hormones in water resources, J. Chromatogr. A 1217 (2010) 4212–4222, https://doi.org/10.1016/j.chroma.2009.11.007.

[36] A. Daneshvar, J. Svanfelt, L. Kronberg, M. Prévost, G.A. Weyhenmeyer, Seasonal variations in the occurrence and fate of basic and neutral pharmaceuticals in a Swedish river–lake system, Chemosphere 80 (2010) 301–309, https://doi.org/10.1016/j.chemosphere.2010.03.060.

[37] M. Mäder, P. Schloss, V. Amberg-Fisher, H_2O_2-formation by NADH-oxidation: A method for H_2O_2-measurement and determination of stoichiometry, Plant Sci. Lett. 23 (1981) 63–69, https://doi.org/10.1016/0304-4211(81)90026-2.

[38] Z. Ye, G.E.M. Schukraft, A. L'Hermitte, Y. Xiong, E. Brillas, C. Petit, I. Sirés, Mechanism and stability of an Fe-based 2D MOF during the photoelectro-Fenton treatment of organic micropollutants under UVA and visible light irradiation, Water Res. 184 (2020) 115986, https://doi.org/10.1016/j.watres.2020.115986.

[39] M.E. Frisch, G. Trucks, H.B. Schlegel, G. Scuseria, M. Robb, J. Cheeseman, G. Scalmani, V. Barone, G. Petersson, H. Nakatsuji, Gaussian 16, Gaussian, Inc., Wallingford, CT, 2016.

[40] A.D. Becke, Density-functional exchange-energy approximation with correct asymptotic behavior, Phys. Rev. A 38 (1988) 3098–3100, https://doi.org/10.1103/PhysRevA.38.3098.

[41] C. Lee, W. Yang, R.G. Parr, Development of the Colle-Salvetti correlation-energy formula into a functional of the electron density, Phys. Rev. B 37 (1988) 785–789, https://doi.org/10.1103/PhysRevB.37.785.

[42] S. Grimme, S. Ehrlich, L. Goerigk, Effect of the damping function in dispersion corrected density functional theory, J Comput Chem 32 (2011) 1456–1465, https://doi.org/10.1002/jcc.21759.

[43] P.C. Hariharan, J.A. Pople, The influence of polarization functions on molecular orbital hydrogenation energies, Theoret. Chim. Acta 28 (1973) 213–222, https://doi.org/10.1007/BF00533485.

[44] S. Miertuš, J. Tomasi, Approximate evaluations of the electrostatic free energy and internal energy changes in solution processes, Chem. Phys. 65 (1982) 239–245, https://doi.org/10.1016/0301-0104(82)85072-6.

[45] C. Hu, C. Huang, B. Peng, Study on the mechanism of photocatalytic degradation of patulin in simulated apple juice, Food Chem. 426 (2023) 136592, https://doi.org/10.1016/j.foodchem.2023.136592.

[46] T. Lu, F. Chen, Multiwfn: A multifunctional wavefunction analyzer, J Comput Chem 33 (2012) 580–592, https://doi.org/10.1002/jcc.22885.

[47] W. Humphrey, A. Dalke, K. Schulten, VMD: Visual molecular dynamics, J. Mol. Graphics 14 (1996) 33–38, https://doi.org/10.1016/0263-7855(96)00018-5.

[48] T. Dong, C. Ling, L. Fu, Y. Xue, Y. Pan, Y. Zhang, C. Zhu, N-doped porous bowl-like carbon with superhigh external surface area for ultrafast degradation of bisphenol A: Key role of site exposure degree, J. Hazard. Mater. 445 (2023) 130562, https://doi.org/10.1016/j.jhazmat.2022.130562.

[49] J.-G. Ku, J.-M. Oh, H. Kwon, J.-W. Lim, High-temperature hydrogen-reduction process for the preparation of low-oxygen Mo powder from MoO_3, Chem. Phys. 42 (2017) 2139–2143, https://doi.org/10.1016/j.ijhydene.2016.09.004.

[50] Y. Zou, J. Li, Q. Peng, Z. Liu, Q. Fu, L. Zhang, Q. Liao, X. Zhu, Tuning the wettability of advanced mesoporous FeNC catalysts for optimizing the construction of the gas/liquid/solid three-phase interface in air-cathodes, Chem. Eng. J. 450 (2022) 138342, https://doi.org/10.1016/j.cej.2022.138342.

[51] Y. Wang, Y. Lin, S. He, S. Wu, C. Yang, Singlet oxygen: Properties, generation, detection, and environmental applications, J. Hazard. Mater. 461 (2024) 132538, https://doi.org/10.1016/j.jhazmat.2023.132538.

[52] H. Zhang, C. Xie, L. Chen, J. Duan, F. Li, W. Liu, Different reaction mechanisms of $SO_4^{\bullet-}$ and $^{\bullet}OH$ with organic compound interpreted at molecular orbital level in Co(II)/peroxymonosulfate catalytic activation system, Water Res. 229 (2023) 119392, https://doi.org/10.1016/j.watres.2022.119392.

[53] J. Xiao, Y. Xie, Q. Han, H. Cao, Y. Wang, F. Nawaz, F. Duan, Superoxide radical-mediated photocatalytic oxidation of phenolic compounds over Ag^+/TiO_2: Influence of electron donating and withdrawing substituents, J. Hazard. Mater. 304 (2016) 126–133, https://doi.org/10.1016/j.jhazmat.2015.10.052.

[54] M. Li, Q. Mei, D. Han, B. Wei, Z. An, H. Cao, J. Xie, M. He, The roles of $HO^{\bullet}$, $ClO^{\bullet}$ and $BrO^{\bullet}$ radicals in caffeine degradation: A theoretical study, Sci. Total Environ. 768 (2021) 144733, https://doi.org/10.1016/j.scitotenv.2020.144733.

[55] J. Qi, X. Yang, P.-Y. Pan, T. Huang, X. Yang, C.-C. Wang, W. Liu, Interface engineering of $Co(OH)_2$ nanosheets growing on the $KNbO_3$ perovskite based on electronic structure modulation for enhanced peroxymonosulfate activation, Environ. Sci. Technol. 56 (2022) 5200–5212, https://doi.org/10.1021/acs.est.1c08806.

[56] K.B. Muchowska, D.J. Pascoe, S. Borsley, I.V. Smolyar, I.K. Mati, C. Adam, G. S. Nichol, K.B. Ling, S.L. Cockroft, Reconciling electrostatic and n→π* orbital contributions in carbonyl interactions, Angew. Chem. 132 (2020) 14710–14716, https://doi.org/10.1002/ange.202005739.